ACS Sustainable Resource Management

pubs.acs.org/acssrm

Article

Steelmaking Wastes as Catalysts for the Circular Conversion of CO_2 to Syngas

Imad E. Aouissi, Maila Danielis, Alessandra Primavera, Giuseppe Giacomini, Alessandro Trovarelli, and Sara Colussi*

Cite This: https://doi.org/10.1021/acssusresmgt.5c00352

Read Online

ACCESS | Metrics & More | Article Recommendations | Supporting Information

ABSTRACT: Reutilizing steel industry waste is increasingly important for reducing its adverse environmental impact and associated disposal costs. Conventional utilization methods offer low added value and are often constrained by the waste's physical and chemical properties. In contrast, catalytic applications can overcome these limitations. This study investigates the catalytic performance of electric arc furnace slag (EAFS), electric arc furnace dust (EAFD), and ladle furnace slag (LFS) in the reverse water−gas shift (RWGS) reaction, which converts CO_2 into CO, a valuable feedstock or reducing agent. Using a CO_2/H_2 gas mixture at a 1:3 ratio, the catalysts were evaluated for their activity, long-term stability over a 24 h isothermal reaction at 750 °C, and tolerance to sulfur following exposure to 150 ppm of H_2S. All materials demonstrated 100% CO selectivity and excellent thermal stability. Notably, EAFD showed only a reversible decrease in activity upon H_2S exposure, significantly outperforming the 3%Pd/Ce/Al_2O_3 reference catalyst, which exhibited an irreversible loss. *In situ* X-ray diffraction (XRD) revealed a correlation between FeO/Fe transformations and the activity of EAFD and EAFS, while LFS showed $CaCO_3$ formation and decomposition as the dominant process. These findings highlight the potential of steelmaking wastes as efficient sulfur-resistant catalysts for large-scale CO_2 utilization via the RWGS reaction.

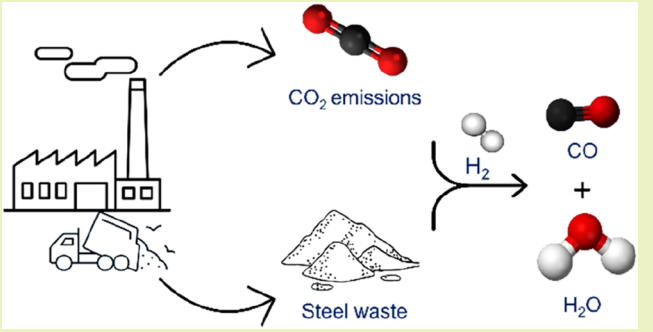

KEYWORDS: *steel waste, steel slag, CO_2 conversion, catalysts, reverse water gas shift reaction*

INTRODUCTION

By the year 2019, global steel production has reached a total of 1.9 billion tons of crude steel.[1] China, Japan, and India have been the leading steel manufacturers and generally steel production is continuously increasing following the global economic growth.[2] As a result of this trend, the steel by-products are also increasing with about 190−290 million tons of steelmaking waste produced annually.[3] Part of the steel waste generated from a primary steelmaking process is the electrical arc furnace slag (EAFS) that is approximately produced in 110−150 kg per ton of steel[4] while also generating 10−20 kg of fine electric arc furnace dust (EAFD).[5] Another typical waste is the ladle furnace slag (LFS) from the secondary steelmaking process, with 20 to 30 kg of ladle slag per ton of steel.[4]

The properties of the steel slag vary depending on the manufacturer, the types of steel produced, and the cooling conditions of the slag. In general, EAFS mainly consists of iron (Fe), calcium (Ca), silicon (Si), and aluminum (Al) oxides, while the minor elements are magnesium (Mg) and manganese (Mn) oxides.[2] In the case of EAFD, it contains iron and zinc oxides as well as some calcium, chlorine, lead, and small concentrations of several others.[5] LFS's main components are Ca, Al, and Si in addition to some Fe and others.[6]

Even though these materials are rich in valuable elements, their large-scale accumulation leads to issues such as resource waste, land occupation, and environmental contamination. Various studies have explored their utilization in different applications. For example, according to Wang and co-workers.[7] they are commonly used in construction to produce aggregates, asphalt, and bricks as well as to enhance strength and partially replace cement. They are also employed as cosolvents, for metal recovery, and in fertilizers and soil improvement. However, their application is limited by poor grindability, low early hydration, and unstable volume due to the presence of free CaO and MgO. On the other hand, these limitations do not affect their use in catalysis.[7] Steel wastes have been proven suitable for catalytic processes and have been

Received: July 23, 2025
Revised: October 16, 2025
Accepted: October 17, 2025

tested in pyrolysis, organic matter degradation, electrocatalysis, and transesterification.[7] Moreover, they are also promising for CO_2 capture due to the presence of free CaO and MgO, as previously demonstrated in both gas-solid carbonation such as the use of EAF dust investigated by Tian and co-workers,[8] and aqueous carbonation, as reported by Omale and co-workers.[9] Considering that the steel industry is responsible for 7−9% of total global CO_2 emissions,[5] integrating the utilization of steel wastes into the steelmaking process as a post-process CO_2 treatment known as carbon capture, utilization, and storage (CCUS) represents an attractive approach worth investigating.

Particularly, the reverse water gas shift (RWGS) reaction is a promising CCUS process in which a CO_2 hydrogenation reaction takes place producing CO gas, commonly known as the syngas component in addition to H_2. The RWGS is an endothermic process, and its reaction enthalpy at 298 K is +41 kJ/mol, hence requiring medium-high temperatures (500 °C−950 °C). One of the advantages of the RWGS is that reactors used in this process can be incorporated into the infrastructure of the steel industry and serve as a clean substitute for the conventional utilization of fossil fuels and biomass sources.[10] Moreover, the produced CO can be used as a reducing agent for iron ores. Syngas, with different H_2:CO ratios, is also a feedstock for chemicals and fuels making the RWGS reaction a major option for revalorizing CO_2 within a circular economy concept, such as when coupled with Fischer-Tropsch process.[11,12]

Typically, noble metals like Pt, Pd, and Rh offer high activity for RWGS but are expensive.[13] Ni is a cheaper alternative but suffers from coke formation susceptibility[13] and, in addition, it promotes a competing exothermic reaction, CO_2 methanation. Cu-based catalysts show lower by-product formation and good activity but suffer from thermal instability.[14] In contrast, Fe-based catalysts are known for their high-temperature stability and CO selectivity.[15,16] Thus, steel wastes containing iron and other metals are suitable alternatives to cheap RWGS catalysts. Moreover, the high CaO content in steel wastes, especially in the case of ladle furnace slag (LFS), is not only beneficial in CO_2 adsorption but also for the RWGS itself, as it has been previously reported that CaO can act as the catalytic phase through Ca Looping (CaL) process, based on the reversible reactions between CaO carbonation and $CaCO_3$ decomposition.[17] This process generally takes place between 650 °C and 900 °C, exhibiting good compatibility with the RWGS reaction.[18] To our knowledge, no studies have reported the use of steel slag as a catalyst for the RWGS reaction, except for one where the waste was chemically modified to use it as a precursor for Fe_3O_4 nanoparticles.[19] Some studies have been focusing more on CO_2 methanation with significant modification of the pristine slag, a procedure that partly contradicts the low-cost catalyst idea and the environmental research purpose. For instance, leached and reduced blast furnace sludge has been investigated by Fuentes and co-workers[20] to attempt selective CO_2 methanation. Another study focused on catalysts based on impregnating an acid-modified blast furnace slag with Ni and Ce for CO_2 conversion into methane.[21]

Thus, assessing the activity of steelmaking wastes, such as electric arc furnace slag (EAFS), electric arc furnace dust (EAFD) and ladle furnace slag (LFS) through the RWGS route with full CO selectivity and with minimum to non-modification is more desirable and can be regarded as a cost-effective alternative to their disposal. In this work, the catalytic performance of these materials is evaluated, and *in-situ* analysis is also performed to get a deeper understanding of how their complex phases change during the reaction, affecting their catalytic activity and stability.

MATERIALS AND METHODS

Materials. Electrical arc furnace slag (EAFS), electrical arc furnace dust (EAFD), and ladle furnace slag (LFS) are steelmaking by-products provided by Danieli & C. S.p.A from the Acciaierie Bertoli Safau steelmaking division. EAFD is used as received, while EAFS and LFS are ground using an automated Fritsch Pulverisette P2 ZrO_2 mortar for 40 and 10 min, respectively, resulting in fine powders (Figure S1). A 3%Pd/Ce/Al_2O_3 catalyst was employed as a reference to evaluate the catalytic performance of the materials. Details on its preparation are reported in the Supporting Information.

Catalytic Test. The catalytic activity of samples for RWGS reaction was tested in a homemade fixed-bed reactor consisting of a quartz tube (i.d. = 12 mm, length = 400 mm) positioned inside a temperature-controlled tubular furnace. A weighed amount (0.2 g) of the catalyst, sieved below 850 μm, was placed in the center of the reactor over a quartz wool bed. Bronkhorst High-Tech Series mass flow controllers were used to continuously feed 300 mL/min of 10% CO_2 and 30% H_2 in N_2 (CO_2/H_2 = 1:3) to run catalytic tests. A fixed WHSV value of 90,000 $mL g_{cat}^{-1} h^{-1}$ was used, while the GHSV values for EAFS, LFS, EAFD, and 3%Pd/Ce/Al_2O_3 were 207,000, 135,000, 63,000, and 41,600 h^{-1} respectively. A 1:3 CO_2/H_2 ratio was chosen to target a 1:2 syngas output. The reaction was carried out between 500 and 830 °C (ramp rate of 10 °C/min), and a K-type thermocouple on top of the catalyst bed was used to measure the reaction temperature. The pressure drop was monitored during the experiments and was always below 3 mbar.

For each sample, two heating-cooling cycles were performed, with the first heating-cooling cycle being taken as the catalyst activation step. Stability tests were performed under the same reaction conditions: after activation, the samples were cooled to 750 °C and maintained for a 24 h isotherm. The sulfur resistance of the best-performing catalyst was assessed at 750 °C by alternating a 1 h treatment with 150 ppm of H_2S in N_2 (under GHSV conditions similar to the catalytic tests) with activity re-evaluation under 10% CO_2 and 30% H_2 in N_2. The outlet gases were analyzed continuously by using an MKS MultiGas 2030 FTIR gas analyzer (MKS Instruments). CO_2 conversion and CO yield were calculated by eqs 1 and 2, respectively.

$$\text{CO}_2\ \text{conversion}\ (\%) = \frac{[\text{CO}_2]\text{in} - [\text{CO}_2]\text{out}}{[\text{CO}_2]\text{in}} \times 100 \quad (1)$$

$$\text{CO yield}\ (\%) = \frac{[\text{CO}]\text{out}}{[\text{CO}_2]\text{in}} \times 100 \quad (2)$$

Characterization. The materials were characterized by different techniques, aiming at gaining as much information as possible about their complex physical-chemical nature. In particular, particle size distribution and surface area and porosity were measured together with their chemical composition and surface functionality. Moreover, X-ray diffraction analysis, thermogravimetric analysis, and H_2 temperature-programmed reduction (H_2-TPR) were also carried out, while CO_2 temperature-programmed desorption (CO_2-TPD) was used to assess the basicity of the samples. Details on the characterization techniques and procedures used are reported in Supporting Information.

***In Situ* XRD.** To examine the phase development throughout the catalytic tests, including the activation cycle, X-ray diffraction (XRD) profiles were collected *in situ* mimicking the conditions of the catalytic tests. The detailed procedure is described in the Supporting Information.

https://doi.org/10.1021/acssusresmgt.5c00352
ACS Sustainable Resour. Manage. XXXX, XXX, XXX−XXX

RESULTS AND DISCUSSION

Materials Composition and Structural Properties. Based on Figure S2, EAFS shows a wide range of particle sizes (1−850 μm), with 90% of them lying below 329 μm. Also, LFS has a similar particle size distribution; however, 90% of the particles are concentrated up to 450 μm. EAFD, on the other hand, exhibits the smallest particle size and the narrowest range (0.3−50 μm), with 90% of the particles measuring less than 14 μm. The specific surface area of the materials varies between 0.8 and 2.3 m^2/g following the order of magnitude: EAFD > LFS > EAFS, as shown in Table S1. The adsorption and desorption isotherms of the samples (Figure S3) exhibit a type IV isotherm with a H3 hysteresis loop, characteristic of mesoporous materials. The pore size distribution, shown in the inset of Figure S3, aligns with the type IV isotherm and primarily falls within the mesoporous range, with the porosity following the same trend of surface area.

Table 1 presents the chemical compositions of EAFS, LFS, and EAFD. The main components of EAFS are Fe, Ca, Si, Mn, and Mg, which are frequently reported.[22] Conversely, Ca makes up 31.7% of the LFS, followed by Al, Fe, Si, and Mg. Although these elements in their oxidic states are often found in LFS, their concentration might differ greatly depending on the source.[23] EAFD is characterized by high content in Fe (17 to 35%) and Zn (4 to 28%).[24] The primary constituents of EAFD in this work are consistently Fe (~23%) and Zn (~25%) followed by Mg, Ca, and Mn as major components.

Table 1. Chemical Compositions for EAFS, LFS, and EAFD Samples

	material		
constituent (%)	EAFS[a]	LFS[a]	EAFD[b]
Fe	25.05	6.46	22.65
Ca	21.91	31.73	4.90
Zn	0.02	0.02	25.31
Al	3.32	8.61	0.70
Si	4.87	3.42	2.00
Mg	3.20	2.58	6.00
Mn	5.37	1.47	3.53
S	0.16	1.25	0.34
Cr	2.00	0.41	0.34
Ti	0.22	0.16	-
P	0.17	0.01	-
Cl	0.10	0.05	0.60
V	0.12	0.03	-
Nb	0.03	0.01	-
Ba	0.04	-	-
S	0.03	0.03	-
Zr	0.02	0.01	-
Cu	0.02	0.02	-
Pt	-	0.02	-
Au	-	0.03	-

[a]Determined by XRF. [b]Determined by ICP-OES.

The XRD patterns of the EAFS, LFS, and EAFD samples are shown in Figure 1. The list of identified compounds with their chemical formulas is reported in Table S2. Each material contains several components, and their full identification is highly complex. Zinc and iron are the primary components of EAFD, in the form of $ZnFe_2O_4$ and ZnO. In the case of LFS, calcium is the main component present as $Ca(OH)_2$, $CaCO_3$, and $Ca_3Al_2O_6$. EAFS consists of $MgFe_2O_4$ and FeO while also containing calcium-based minerals like $CaCO_3$, $Ca_2(Al,Fe)_2O_5$, and Ca_2SiO_4.

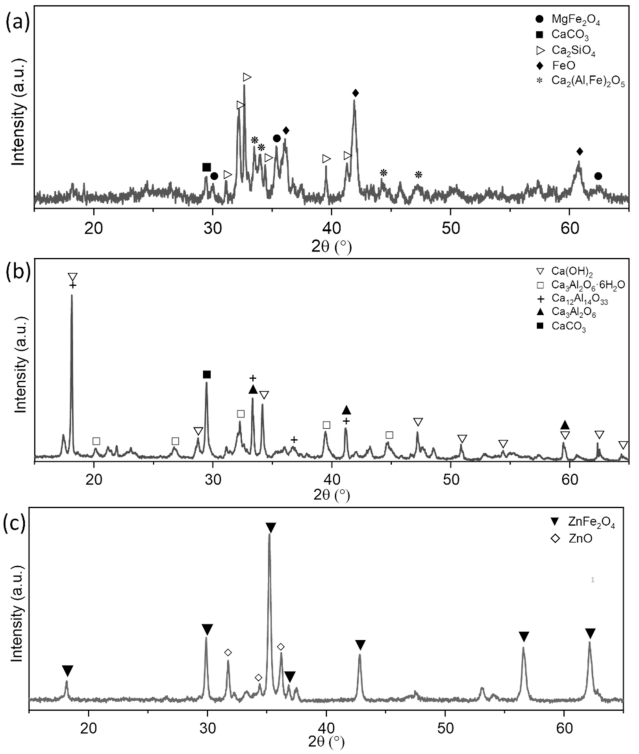

Figure 1. XRD patterns of (a) EAFS, (b) LFS, and (c) EAFD.

The ATR spectra of the EAFS, LFS, and EAFD samples are presented in Figure S4. The absorption band at 1455 cm^{-1} in all spectra is due to calcium carbonate, with additional calcite's common bands at 874 and 712 cm^{-1}.[25]

In the EAFS sample, bands at 991, 843, and 497 cm^{-1} are assigned to Si−O vibrations of Ca_2SiO_4.[26] For the LFS sample, the bands at 511, 793, and 903 cm^{-1} are attributed to Al−O−Al symmetric stretching and to Al−O stretching and bending in calcium aluminates.[27] In addition to calcite, the LFS displays a sharp absorption band around 3640 cm^{-1}, attributed to the O−H stretching vibrations of portlandite.[27] EAFD shows a band at 520 cm^{-1} corresponding to Zn−O bonds, and the bands at 1193 and 1404 cm^{-1}, correlated to sulfate ions (SO_4^{2-}) vibrations and carbonate ions (CO_3^{2-}).[28] Additionally, peaks within the 900−1200 cm^{-1} range are generally attributed to Si−O vibrations.[29,30]

Overall, combining XRD and ATR with elemental analysis confirms and integrates the identification of the main compounds present in each sample. For instance, in the EAFD sample, while ATR confirms the Zn−O bond, XRD identifies the main crystalline phases such as $ZnFe_2O_4$ and ZnO. ATR also detects carbonates and sulfates, which are not detected by XRD being likely amorphous, and also confirms the presence of Si, supporting the XRF results. In the case of LFS, ATR bands distinctively confirm Ca-rich phases supporting the XRD findings. The primary components of EAFS are Fe, Ca, and Al, as demonstrated by XRF, and XRD identified their corresponding crystalline phases. The ATR analysis highlights the presence of $CaSiO_4$ and $CaCO_3$.

Activity for CO_2 Hydrogenation. The catalytic activity of EAFD, EAFS, and LFS was assessed and compared with a

https://doi.org/10.1021/acssusresmgt.5c00352
ACS Sustainable Resour. Manage. XXXX, XXX, XXX−XXX

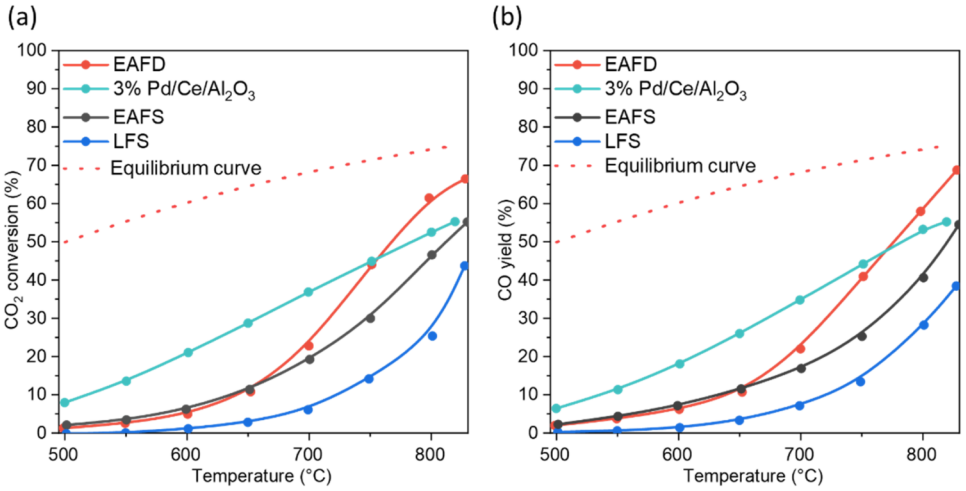

Figure 2. Comparison of (a) catalytic CO_2 conversion, (b) CO yield for EAFD, EAFS, LFS, and 3%Pd/Ce/Al_2O_3 catalysts.

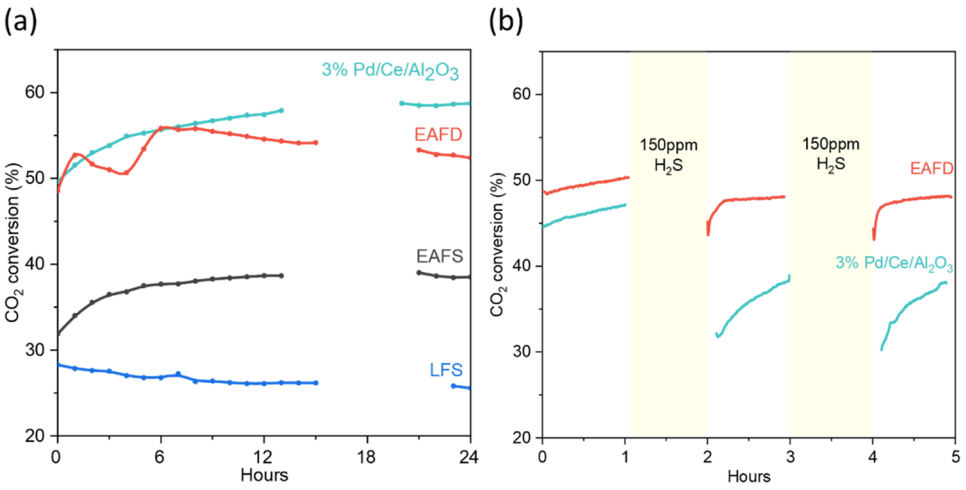

Figure 3. Comparison at 750 °C: (a) catalytic stability for EAFD, EAFS, LFS, and 3%Pd/Ce/Al_2O_3 catalysts, and (b) H_2S resistance evaluation for EAFD and 3%Pd/Ce/Al_2O_3.

reference catalyst, 3%Pd/10%Ce/Al_2O_3, as shown in Figure 2a. The EAFD sample exhibited a crossing point at 750 °C, where its performance outperformed that of the reference catalyst. The selectivity to CO remained approximately 100% under all conditions, as shown in Figure 2b, confirming that the RWGS reaction proceeded selectively with only trace amounts of methane produced (Figure S5). It is also noteworthy to observe that CO_2 consumption rate normalized by surface area is much higher on EAFS due to its extremely low surface area (Figure S6).

Figure 3a presents the stability behavior of the EAFD, EAFS, LFS, and 3%Pd/Ce/Al_2O_3 catalysts during a 24 h reaction at 750 °C. All catalysts demonstrated CO_2 conversion without significant deactivation, except for EAFD and EAFS where an initial increase in the level of CO_2 conversion was observed. For EAFD, the increase was faster, followed by a slight decrease and another steep increase. This transient behavior, which proved to be reproducible, occurred within the first 6 h of test, and it might be related to some material reconstruction, where different oxide/metal species form during the reaction following a certain induction time. This phenomenon is likely confined at a surface-subsurface level since it could not be followed by *in situ* XRD analysis as explained in the following. After 6 h, all samples remained reasonably stable up to 24 h.

Figure 3b illustrates the impact of 150 ppm of H_2S on the CO_2 conversion of the top-performing catalyst, EAFD, compared to the reference 3%Pd/Ce/Al_2O_3. When H_2S was removed from the gas feed, EAFD exhibited a temporary drop in conversion with a fast recovery that brought back the conversion at a slightly lower value with respect to the fresh catalyst (50% vs 48%), demonstrating a high resistance to sulfur poisoning. Possibly, this might be attributed to the fraction of alkaline elements acting as sacrificial adsorbents during sulfur exposure, while also allowing for fast desorption and reactivation when the reactive feed is restored. In contrast, the reference catalyst experienced an irreversible performance loss, and its recovery after H_2S removal was much slower. These findings suggest that catalysts derived from steelmaking waste can offer excellent stability and sulfur resistance.

Redox Behavior. Figure 4 displays the H_2-TGA analysis of samples, revealing different weight loss profiles due to their characteristic compositions. As shown in Figure 4a, EAFD shows limited water loss compared to the other materials. The DTG curve indicates minor weight loss starting above 430 °C suggesting the initial reduction of $ZnFe_2O_4$ that later on might

https://doi.org/10.1021/acssusresmgt.5c00352
ACS Sustainable Resour. Manage. XXXX, XXX, XXX−XXX

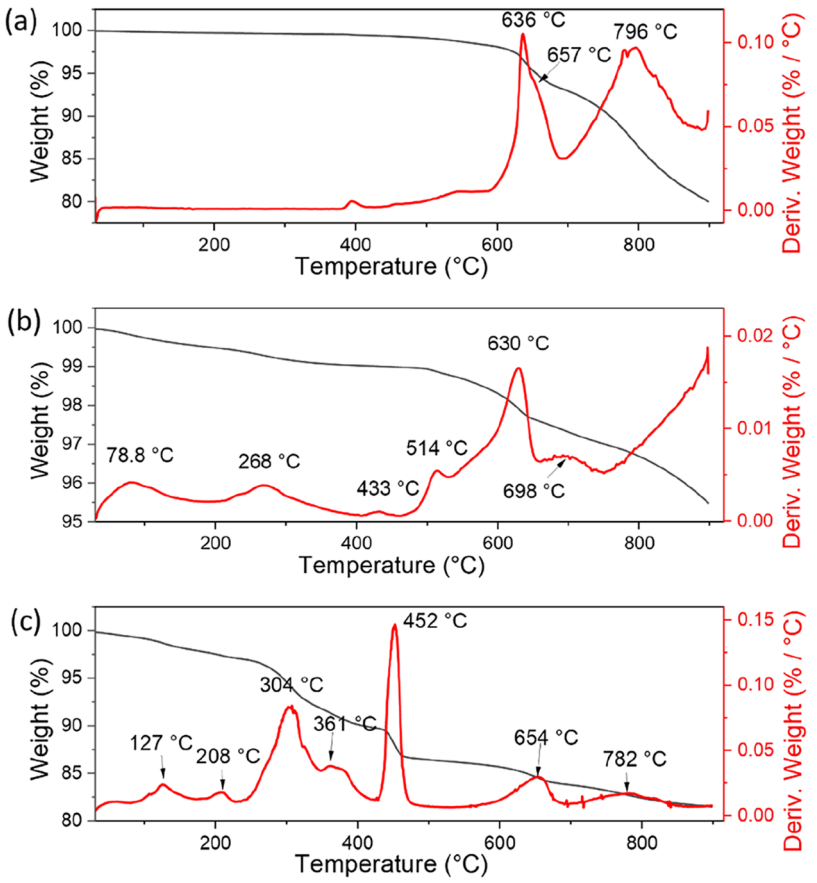

Figure 4. TGA and DTG curves of (a) EAFD, (b) EAFS, and (c) LFS.

be overlapping with the peak maximum at 636 °C, attributed to the reduction of Fe_3O_4 to FeO, in agreement with literature findings.[31] The peak at 796 °C is likely due to the sublimation of metallic zinc. Additionally, weight loss may also result from the consumption of carbon impurities in the material, which can facilitate the reduction of ZnO.[32] For EAFS (Figure 4b), the observed weight loss of up to 400 °C is attributed to the dehydration of several mineral components. Above 400 °C, weight changes suggest the onset of reduction, with the peak maximum at approximately 630 °C attributed to the reduction of spinel $MgFe_2O_4$, observed in this range due to the presence of large particles formed for the exposure of the pristine material to the high temperature of the electrical arc furnace.[33] The TGA curve (Figure 4c) for the LFS sample show a broad weight loss between 100 and 500 °C. According to the DTG curve, the peak at approximately 300 °C is attributed to the dehydration of $Ca_3Al_2O_6{\cdot}6H_2O$.[27] A sharp peak at 452 °C corresponds to the decomposition of $Ca(OH)_2$ into CaO.[34] As for the third peak, which is observed at 654 °C, it is mainly a decarbonization of $CaCO_3$.

The H_2-TPR analysis (Figure 5) provides additional valuable insights into the reducibility of the samples, and the results obtained here also demonstrate its potential as a useful tool for a preliminary evaluation of steel wastes in light of their catalytic application. EAFD exhibits the lowest reduction temperature and the highest H_2 consumption, indicating higher reducibility that is likely responsible for the higher catalytic activity observed for this sample. The peak at 460 °C is related to the reduction of $ZnFe_2O_4$ to Fe_3O_4 followed by the predominant peak at 630 °C corresponding to the reduction of Fe_3O_4 to

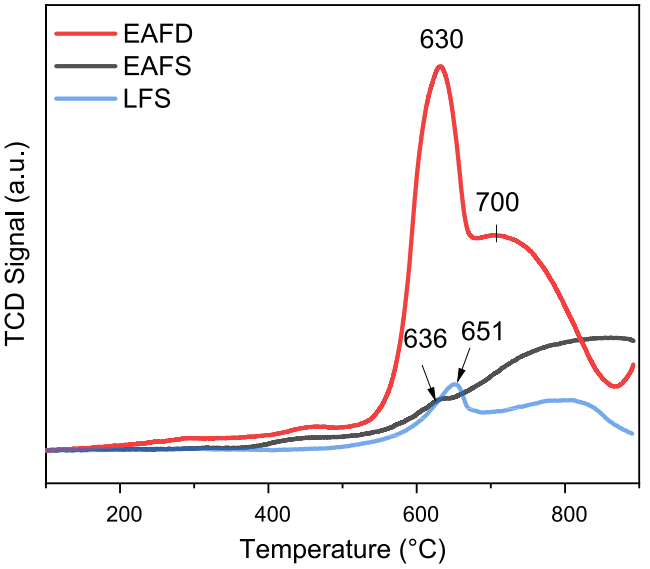

Figure 5. H_2-TPR profiles of EAFS, LFS, and EAFD samples.

FeO, and a broad peak at 700 °C, attributed to the reduction of FeO to Fe.[35] Notably, the absence of a peak at 800 °C, in contrast to the TGA results, confirms the loss of organic components and the sublimation of metallic zinc. EAFS is the second in terms of reducibility, based on both H_2 consumption and the initial reduction temperature. The reduction of $MgFe_2O_4$ to FeO, MgO, and Fe is responsible for the material's redox behavior. In agreement with TGA analysis, the

https://doi.org/10.1021/acssusresmgt.5c00352
ACS Sustainable Resour. Manage. XXXX, XXX, XXX−XXX

hydrogen consumption at 636 °C is associated with the reduction of $MgFe_2O_4$.[33] This is followed by a larger peak, likely due to the reduction of FeO to Fe. Despite having the highest iron content, EAFS contains iron-based minerals such as $Ca_2(Al,Fe)_2O_5$, which require a higher reduction temperature. LFS exhibits the lowest H_2 consumption, likely due to its low iron concentration. The first peak at 651 °C is primarily attributed to the hydrogenation of $CaCO_3$ and may coincide with the reduction of iron oxides in the sample.

CO_2-TPD. The material's basic properties are crucial for its catalytic performances in terms of stability, particularly in preventing carbon buildup and in promoting the activation of acidic CO_2 molecules. As shown in Figure 6, the CO_2-TPD analysis reveals the presence of three types of basic sites. The temperature of CO_2 desorption depends on the strength of the basic sites, allowing to identify them as weak (<300 °C), medium (300−600 °C), and strong ones (>600 °C). The LFS sample, which has the highest concentration of calcium and alumina, exhibits basic characteristics mostly observed between 400 and 600 °C,[36] and it is also the sample that shows the highest amount of basic sites. EAFD and EAFS display a much lower content of basic sites with a less defined distribution. At higher temperatures, the presence of strong basic sites follows the order: EAFD > LFS > EAFS. Since the materials' activity is observed to be higher at elevated temperatures, the presence of strong basic sites likely affects catalytic activity, in addition to the primary influence of iron content. On the contrary, medium and weak basic sites likely have a limited impact on CO_2 activation at high temperatures. These evidences highlight the relevance of CO_2-TPD experiments as a tool to complement H_2-TPR for the assessment of steel wastes as potential CO_2 valorization catalysts.

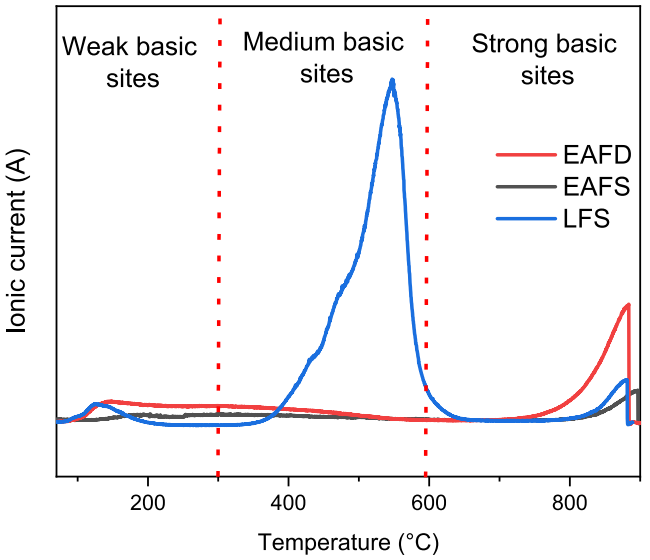

Figure 6. CO_2-TPD profiles of EAFS, LFS, and EAFD samples.

***In Situ* XRD Analysis.** To further look into the main factors affecting the catalytic performance, the phase development of LFS, EAFS, and EAFD throughout the activation cycle and the second cycle at temperatures ranging from 550 to 830 °C was followed by *in situ* XRD, illustrated in Figure 7. During the first (activation) cycle on the LFS sample, the $Ca_3Al_2O_6{\cdot}6H_2O$ is fully dehydrated at 550 °C, as seen in Figure 7a, whilst the peaks ascribed to $Ca_3Al_2O_6$ increase in intensity and, consequently, in content. Similarly, $Ca(OH)_2$ decomposes, which is likewise connected to the formation of CaO. From 550 to 650 °C, a steady rise in $CaCO_3$ intensity is also observed, demonstrating the range of CO_2 absorption by CaO. $CaCO_3$ then also starts to decompose to produce CaO. With the exception of the dehydration step, the second cycle shows a similar behavior, and the clear formation of CaO at 700 °C explains the sharp rise in CO_2 conversion, suggesting that it is the primary active phase.

The EAFS sample in Figure 7b displays the reduction of $MgFe_2O_4$, beginning at 550 °C and completely breaking down into FeO and Fe between 600 and 650 °C, supporting the findings of the H_2-TPR investigation. When the FeO content reaches its maximum at 650 °C, it undergoes partial reduction to metallic Fe. The second cycle is started after cooling to 550 °C, and the reduction of FeO to metallic Fe continues until

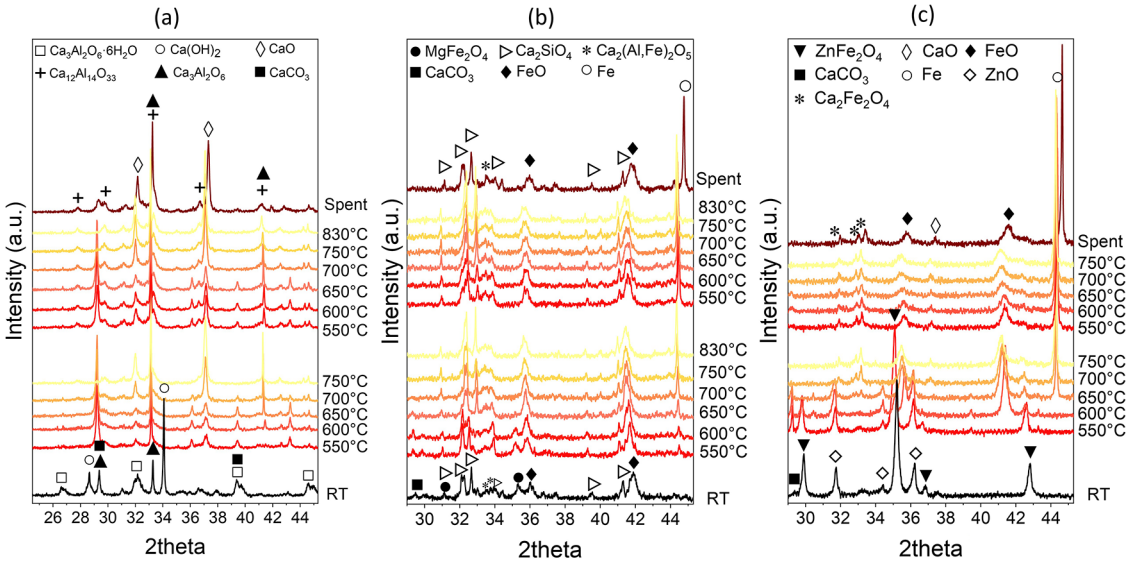

Figure 7. *In situ* XRD patterns showing the temperature-dependent phase evolution of (a) LFS, (b) EAFS, and (c) EAFD samples during the 1st and 2nd cycles of CO_2 hydrogenation.

https://doi.org/10.1021/acssusresmgt.5c00352
ACS Sustainable Resour. Manage. XXXX, XXX, XXX−XXX

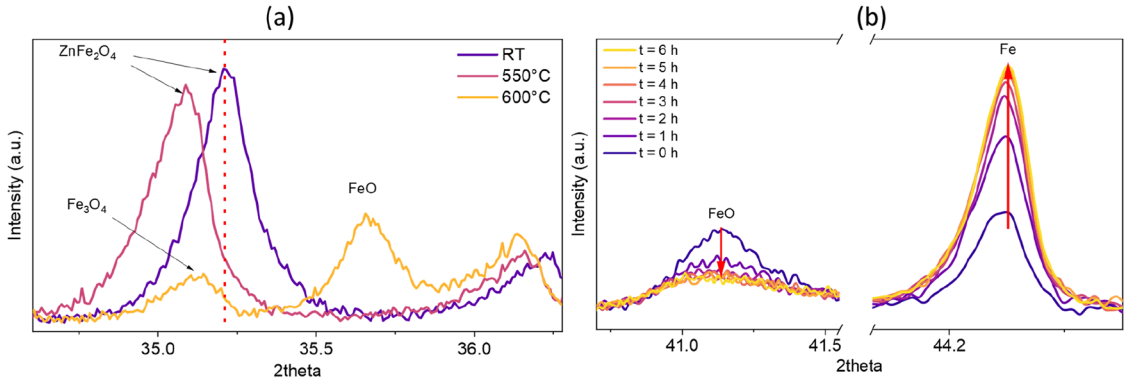

Figure 8. *In situ* XRD patterns obtained for (a) during the first cycle of CO_2 hydrogenation and (b) over 6 h during CO_2 hydrogenation on the EAFD sample at constant T = 750 °C.

700 °C. The Fe content, however, somewhat declines above this temperature. This might be explained by the presence of CO_2 at high temperatures, which can cause partial re-oxidation to FeO. Lastly, Ca_2SiO_4 goes through an unidentified phase transition to an unstable intermediate before cooling and returning to the stable larnite phase.

On EAFD, as represented in Figure 7c, initially, carbonation of calcium to $CaCO_3$ starts followed by full decomposition at 700 °C while also CaO becomes visible at 700 °C. Also, $CaFe_2O_4$ peaks appear at 650 °C suggesting that part of calcium and iron react. The reduction of $ZnFe_2O_4$ begins around 550 °C, leading to the formation of FeO and ZnO. While peaks shift to lower angles is generally due the temperature increase, an observed slight shift of the diffraction peaks to higher angles at 600 °C (Figure 8a) indicates lattice contraction, which can be attributed to the formation of Fe_3O_4. Fe_3O_4 is characterized by smaller interplanar spacings compared to $ZnFe_2O_4$, resulting in the rightward shift of diffraction peaks. ZnO reduction starts at 650 °C to be fully reduced and evaporated after 700 °C. Qi and Hu.[37] reported that the presence of metals with ZnO can affect the loss of ZnO dramatically, and in the case of Fe, due to its high oxophilicity, it can accelerate the ZnO loss. In the second cycle, the main components are Fe and FeO, behaving similarly to EAFS in which FeO is continuously reduced to Fe up to 700 °C and then at higher temperature slightly oxidized. However, at 650 °C, FeO decreased in intensity while Fe remained unchanged, and this can be explained by another factor, i.e., the formation of $CaFe_2O_4$ that occurs at a similar temperature. Moreover, it can be shown that $CaCO_3$ in the second cycle is barely visible indicating that it was consumed to form $CaFe_2O_4$.

These results indicate that the higher total metallic Fe formed is the reason for EAFD's superior activity over EAFS at higher temperatures. The Fe content calculated via eq S1 shows that in EAFD it increases to 20%, whereas in the case of EAFS, it is only 9%.

The *in situ* XRD patterns presented in Figure 8b correspond to the stability test conducted under the same reaction conditions as those for the previously mentioned stability test in the reactor setup at 750 °C on the EAFD sample. The results indicate a steady reduction of FeO to metallic Fe, primarily occurring within the first 2 h, which may explain the gradual increase in the rate of CO_2 conversion observed during the stability test in the same time range (Figure 3a). However, the following drop in CO_2 conversion could not be related to other phase changes detected using this bulk technique, suggesting that additional investigations are required to fully understand this phenomenon, which might likely take place at the surface-subsurface level.

CONCLUSIONS

In this study, three types of steel waste materials, containing various metal oxides, were evaluated as catalysts for the RWGS reaction without chemical modification. Their catalytic activity, CO selectivity, thermal stability, and H_2S resistance were assessed. Among them, EAFD demonstrated superior performance, surpassing the reference 3%Pd/Ce/Al_2O_3 catalyst at temperatures above 750 °C, achieving 58% CO_2 conversion and an approximately 100% CO yield. Additionally, EAFD, along with EAFS and LFS, exhibited excellent thermal stability over 24 h at 750 °C. Notably, EAFD showed exceptional resistance to H_2S poisoning, with only a slight drop in performance, which was fully recovered upon H_2S removal, highlighting its potential for large-scale CO_2 utilization processes in demanding industrial applications.

In situ XRD analysis provided valuable insights into the phase transitions occurring during CO_2 hydrogenation, identifying Fe/FeO as the active phase in EAFD and EAFS, while CaO was the dominant active phase in LFS. Remarkably, EAFD exhibited a higher proportion of metallic Fe compared with EAFS, despite having a lower total iron content. This can be attributed to its superior reducibility, as observed by H_2-TPR and H_2-TGA, along with the possible contribution of its higher concentration of strong basic sites, which may further enhance the catalytic performance. Remarkably, the results obtained in this work highlight that relatively simple characterization techniques, such as H_2-TPR and CO_2-TPD can be valuable tools to assess the relevant properties behind the catalytic activity trend observed. This seems particularly promising also for an *a priori* screening of steel wastes for CO_2 valorization applications, where it would be very useful to rely on a fast experimental approach without the need for a full characterization of such complex materials. Overall, the combination of catalytic results and *in situ* characterization analyses highlights the potential of using waste materials, such as dust from steel manufacturing, as a cost-effective and S-resistant catalyst for CO_2 utilization. Further performance enhancement might be carried out by selectively targeting the activation of metallic Fe in the waste materials.

https://doi.org/10.1021/acssusresmgt.5c00352
ACS Sustainable Resour. Manage. XXXX, XXX, XXX−XXX

■ ASSOCIATED CONTENT

Supporting Information

The Supporting Information is available free of charge at https://pubs.acs.org/doi/10.1021/acssusresmgt.5c00352.

Details on materials preparation and characterization procedures; an image showing the material's physical appearance before and after grinding; particle size distribution graph; table reporting surface area and porosity of samples; N_2 adsorption−desorption isotherms; table reporting chemical formulas and nomenclatures of the components observed by XRD analysis; ATR-FTIR spectra of samples; a comparison of CH_4 yield in the RWGS reaction; CO_2 consumption rates normalized per surface area of samples (PDF)

■ AUTHOR INFORMATION

Corresponding Author

Sara Colussi − *Polytechnic Department of Engineering and Architecture, University of Udine, Udine 33100, Italy;* orcid.org/0000-0001-5316-1746; Email: sara.colussi@uniud.it

Authors

Imad E. Aouissi − *Polytechnic Department of Engineering and Architecture, University of Udine, Udine 33100, Italy*

Maila Danielis − *Polytechnic Department of Engineering and Architecture, University of Udine, Udine 33100, Italy;* orcid.org/0000-0001-8469-9282

Alessandra Primavera − *Danieli & C. Officine Meccaniche S.p.A., Buttrio, Udine 33042, Italy*

Giuseppe Giacomini − *Acciaierie Bertoli Safau SpA, Pozzuolo del Friuli, Udine 33050, Italy*

Alessandro Trovarelli − *Polytechnic Department of Engineering and Architecture, University of Udine, Udine 33100, Italy;* orcid.org/0000-0002-1396-4031

Complete contact information is available at: https://pubs.acs.org/10.1021/acssusresmgt.5c00352

Author Contributions

All authors contributed to the preparation of the manuscript and approved its final version. I.E.A.: Investigation, data curation, visualization, writing—original draft. M.D.: Conceptualization, supervision, writing—review and editing; A.P.: Supervision, funding acquisition, writing—review and editing; G.G.: Resources, writing—review and editing; A.T.: Funding acquisition, resources, writing—review and editing; S.C.: Conceptualization, supervision, writing—review and editing.

Funding

The work has been supported by the NRRP Mission 4, Component 2, Investment/Sub-investment 3.3, and by Danieli & C. Officine Meccaniche S.p.A., which provided financial support for the PhD fellowship (CUP: G23D22000790005).

Notes

The authors declare no competing financial interest.

■ ACKNOWLEDGMENTS

The authors thank the University of Udine and Danieli & C. Officine Meccaniche S.p.A. for providing research facilities.

■ REFERENCES

(1) Medarac, H.; Moya, J.; Somers, J. Production costs from iron and steel industry in the EU and third countries 2020 https://op.europa.eu/s/z6Wd. (Accessed July 5, 2025).

(2) Teo, P. T.; Zakaria, S. K.; Salleh, S. Z.; Taib, M. A. A.; Sharif, N. M.; Seman, A. A.; Mohamed, J. J.; Yusoff, M.; Yusoff, A. H.; Mohamad, M.; Masri, M. N.; Mamat, S. Assessment of Electric Arc Furnace (EAF) Steel Slag Waste's Recycling Options into Value Added Green Products: A Review. *Metals* **2020**, *10* (10), No. 1347.

(3) Mineral Commodity Summaries 2019 2019 https://pubs.usgs.gov/publication/70202434. (Accessed July 5, 2025).

(4) Araos, P.; Aponte, D.; Barra, M. Ladle furnace slag as a new source of supplementary cementitious material: Evaluating long-term performance and environmental impact in Portland cement systems. *J. Build. Eng.* **2024**, *95*, No. 109995.

(5) Frilund, C.; Kotilainen, M.; Lorenzo, J. B.; Lintunen, P.; Kaunisto, K. Steel Manufacturing EAF Dust as a Potential Adsorbent for Hydrogen Sulfide Removal. *Energy Fuels* **2022**, *36* (7), 3695−3703.

(6) Wu, L.; Li, H.; Mei, H.; Rao, L.; Wang, H.; Lv, N. Generation, utilization, and environmental impact of ladle furnace slag: A minor review. *Sci. Total Environ.* **2023**, *895*, No. 165070.

(7) Wang, F. P.; Liu, T. J.; Cai, S.; Gao, D.; Yu, Q.; Wang, X. M.; Wang, Y. T.; Zeng, Y. N.; Li, J. G. A Review of Modified Steel Slag Application in Catalytic Pyrolysis, Organic Degradation, Electrocatalysis, Photocatalysis, Transesterification and Carbon Capture and Storage. *Appl. Sci.* **2021**, *11* (10), No. 4539.

(8) Tian, S.-c.; Jiang, J.-g.; Li, K.-m.; Yan, F.; Chen, X.-j. Performance of steel slag in carbonation−calcination looping for CO_2 capture from industrial flue gas. *RSC Adv.* **2014**, *4* (14), 6858−6862.

(9) Omale, S. O.; Choong, T. S. Y.; Abdullah, L. C.; Siajam, S. I.; Yip, M. W. Utilization of Malaysia EAF slags for effective application in direct aqueous sequestration of carbon dioxide under ambient temperature. *Heliyon* **2019**, *5* (10), No. e02602.

(10) González-Castaño, M.; Dorneanu, B.; Arellano-García, H. The reverse water gas shift reaction: a process systems engineering perspective. *React. Chem. Eng.* **2021**, *6* (6), 954−976.

(11) Choi, S.; Sang, B.-I.; Hong, J.; Yoon, K. J.; Son, J.-W.; Lee, J.-H.; Kim, B.-K.; Kim, H. Catalytic behavior of metal catalysts in high-temperature RWGS reaction: In-situ FT-IR experiments and first-principles calculations. *Sci. Rep.* **2017**, *7* (1), No. 41207.

(12) Tamakuwala, K. N.; Kennedy, R. P.; Li, C. S.; Mutz, B.; Boller, P.; Bare, S. R.; Kanan, M. W. Intermediate-Temperature Reverse Water−Gas Shift under Process-Relevant Conditions Catalyzed by Dispersed Alkali Carbonates. *JACS Au* **2025**, *5* (3), 1083−1089.

(13) Zhou, C.; Zhang, J.; Fu, Y.; Dai, H. Recent Advances in the Reverse Water−Gas Conversion Reaction. *Molecules* **2023**, *28* (22), No. 7657.

(14) Yue, H.; Zhao, Y.; Zhao, S.; Wang, B.; Ma, X.; Gong, J. A copper-phyllosilicate core-sheath nanoreactor for carbon−oxygen hydrogenolysis reactions. *Nat. Commun.* **2013**, *4* (1), No. 2339.

(15) Kim, D. H.; Han, S. W.; Yoon, H. S.; Kim, Y. D. Reverse water gas shift reaction catalyzed by Fe nanoparticles with high catalytic activity and stability. *J. Ind. Eng. Chem.* **2015**, *23*, 67−71.

(16) Li, Z.; Liu, J.; Shi, R.; Waterhouse, G. I. N.; Wen, X.-D.; Zhang, T. Fe-Based Catalysts for the Direct Photohydrogenation of CO_2 to Value-Added Hydrocarbons. *Adv. Energy Mater.* **2021**, *11* (12), No. 2002783.

(17) Zhang, X.; Liu, W.; Peng, P.; Zhang, Z.; Du, Q.; Shi, J.; Deng, L. A dual functional sorbent/catalyst material for in-situ CO_2 capture and conversion to ethylene production. *Fuel* **2023**, *351*, No. 128701, DOI: 10.1016/j.fuel.2023.128701.

(18) Chen, J.; Jiang, Y.; Liu, X.; Xia, W.; Huang, A.; Zong, J.; Wang, Z.; Qian, B.; Donat, F. One-step synthesis of CaO/CuO composite pellets for enhanced CO_2 capture performance in a combined Ca/Cu looping process via a facile gel-casting technique. *Sep. Purif. Technol.* **2024**, *328*, No. 125057, DOI: 10.1016/j.seppur.2023.125057.

(19) Kumar, V.; Lamba, N. K.; Baig, A.; Kaushik, J.; Jha, T.; Sonal; Sonkar, S. K. Utilization of steel industry waste derived magnetic iron-oxide nanoparticles for reverse water gas shift reaction. *Chem. Eng. J.* **2023**, *477*, No. 147027.
(20) Fuentes, I.; Bernales, N.; Ulloa, C.; García, X. Kinetics of CO_2 methanation using a Fe-bearing blast furnace sludge as catalytic precursor. *Catal. Today* **2022**, *394*−*396*, 198−207.
(21) Chen, X.; He, Y.; Cui, X.; Liu, L. High value utilization of waste blast furnace slag: New Ni-CeO_2/hBFS catalyst for low temperature CO_2 methanation. *Fuel* **2023**, *338*, No. 127309, DOI: 10.1016/j.fuel.2022.127309.
(22) Kishore, K.; Sheikh, M. N.; Hadi, M. N. S. A critical analysis of electric arc furnace (EAF) slag for sustainable geopolymer concrete production. *Mater. Today Sustainability* **2025**, *29*, No. 101064.
(23) Ouffa, N.; Benzaazoua, M.; Trauchessec, R.; Belem, T.; Taha, Y.; Diliberto, C. Potential Reuse of Ladle Furnace Slag as Cementitious Material: A Literature Review of Generation, Characterization, and Processing Methods. *Minerals* **2024**, *14* (12), No. 1204.
(24) Suetens, T.; Guo, M.; Van Acker, K.; Blanpain, B. Formation of the $ZnFe_2O_4$ phase in an electric arc furnace off-gas treatment system. *J. Hazard. Mater.* **2015**, *287*, 180−187.
(25) Hajji, S.; Turki, T.; Boubakri, A.; Amor, M. B.; Mzoughi, N. Study of cadmium adsorption onto calcite using full factorial experiment design. *Desalin. Water Treat.* **2017**, *83*, 222−233.
(26) Timón, V.; Torrens-Martin, D.; Fernández-Carrasco, L. J.; Martínez-Ramírez, S. Infrared and Raman vibrational modelling of β-C_2S and C_3S compounds. *Cem. Concr. Res.* **2023**, *169*, No. 107162, DOI: 10.1016/j.cemconres.2023.107162.
(27) Luo, Y.; Klima, K. M.; Brouwers, H. J. H.; Yu, Q. Effects of ladle slag on Class F fly ash geopolymer: Reaction mechanism and high temperature behavior. *Cem. Concr. Compos.* **2022**, *129*, No. 104468.
(28) Nikolić, I.; Đurović, D.; Marković, S.; Veselinović, L.; Janković-Častvan, I.; Radmilović, V. V.; Radmilović, V. R. Alkali activated slag cement doped with Zn-rich electric arc furnace dust. *J. Mater. Res. Technol.* **2020**, *9* (6), 12783−12794.
(29) Dehnavi, M.; Ebadi, T.; Khorsandi, B.; Dezvareh, G. Investigating the utilization of electric arc furnace dust in landfill construction: A cleaner production approach. *J. Cleaner Prod.* **2024**, *470*, No. 143350.
(30) Martins, F. M.; dos Reis Neto, J. M.; Cunha, C. J. d., Mineral phases of weathered and recent electric arc furnace dust. *J. Hazard. Mater.* **2008**, *154* (1), 417−425.
(31) Hoffelner, F. Kinetic Aspects of the Selective Reduction of Zinc Ferrite with H_2 in the Processing of Electric Arc Furnace Dust 2022 https://pure.unileoben.ac.at/en/publications/kinetic-aspects-of-the-selective-reduction-of-zinc-ferrite-with-h. (Accessed July 11, 2025).
(32) Almeida, M. M.; Saczk, A. A.; da Silva Felix, F.; Penido, E. S.; Santos, T. A. R.; de Souza Teixeira, A.; Magalhães, F. Characterization of electric arc furnace dust and its application in photocatalytic reactions to degrade organic contaminants in synthetic and real samples. *J. Photochem. Photobiol., A* **2023**, *438*, No. 114585.
(33) Yang, M.; Li, G.; Li, H.; Ding, J.; Wang, Y.; Li, L. Growth kinetic control over $MgFe_2O_4$ to tune Fe occupancy and metal−support interactions for optimum catalytic performance. *CrystEngComm* **2021**, *23* (13), 2538−2546.
(34) Zhao, B.; Wang, J.; Zhu, D.; Song, G.; Yang, H.; Chen, L.; Sun, L.; Yang, S.; Guan, H.; Xie, X. Adsorption Characteristics of Gas Molecules (H_2O, CO_2, CO, CH_4, and H_2) on CaO-Based Catalysts during Biomass Thermal Conversion with in Situ CO_2 Capture. *Catalysts* **2019**, *9* (9), No. 757, DOI: 10.3390/catal9090757.
(35) Sarifuddin, W. S.; Mahadi, A. H.; Hussin, M. R.; Masri, M. K. Z.; Holilah; Prasetyoko, D.; Bahruji, H. Cu doped $ZnFe_2O_4$ photocatalysts for enhanced hydrogen production and dye degradation in the visible region. *J. Photochem. Photobiol., A* **2024**, *453*, No. 115658.
(36) Kholkina, E.; Kumar, N.; Ohra-aho, T.; Lehtonen, J.; Lindfors, C.; Perula, M.; Peltonen, J.; Salonen, J.; Murzin, D. Y. Synthesis and Characterization of Novel Catalytic Materials Using Industrial Slag: Influence of Alkaline Pretreatment, Synthesis Time and Temperature. *Top. Catal.* **2019**, *62* (7−11), 738−751.
(37) Qi, J.; Hu, X. The loss of ZnO as the support for metal catalysts by H_2 reduction. *Phys. Chem. Chem. Phys.* **2020**, *22* (7), 3953−3958.

https://doi.org/10.1021/acssusresmgt.5c00352
ACS Sustainable Resour. Manage. XXXX, XXX, XXX−XXX